RSC Advances

PAPER

View Article Online
View Journal | View Issue

Cite this: RSC Adv., 2016, 6, 13757

Quasi-one-dimensional graphene nanoribbon-supported MoS_2 nanosheets for enhanced hydrogen evolution reaction†

Huahao Gu,[a] Longsheng Zhang,[a] Yunpeng Huang,[a] Youfang Zhang,[a] Wei Fan*[b] and Tianxi Liu*[ab]

Electrolysis of water is a sustainable and environmentally friendly way to produce hydrogen, which has motivated people to develop efficient and earth-abundant electrocatalysts that minimize energy consumption. Herein, graphene nanoribbon@MoS_2 (GNR@MoS_2) hybrids with hierarchical structure have been facilely fabricated as efficient electrocatalysts for the hydrogen evolution reaction (HER). Derived from longitudinally unzipping of multi-walled carbon nanotubes, GNR sheets can provide a greater surface area for the decoration of MoS_2, which not only stems from the outer wall sheets, but also from the additional exfoliated inner wall space, as well as from the unique ribbon edges. Furthermore, the interconnected GNR sheets can form a conductive pathway for fast electron transportation and an open structure for convenient electrolyte permeation. As a consequence, the GNR@MoS_2 hybrids exhibit excellent electrochemical activity as HER catalysts with a low onset potential of −0.11 V *vs.* the reversible hydrogen electrode and a small Tafel slope of 43.4 mV per decade. The outstanding electrocatalytic performance of the GNR@MoS_2 hybrids can be ascribed to their unique hierarchical architecture with numerous active sites, as well as synergistic effects between the electrocatalytic MoS_2 nanosheets and conductive GNR framework, making them promising materials for future electrocatalysts in the HER.

Received 19th December 2015
Accepted 21st January 2016

DOI: 10.1039/c5ra27180k

www.rsc.org/advances

1. Introduction

The rapid developing society has urgently called for renewable and environmentally friendly energy sources as substitution for fossil fuels.[1] It is universally acknowledged that hydrogen is an ideal energy carrier in the future world.[2] Recently, electrocatalytic[3,4] and photocatalytic[5–8] production of hydrogen from water splitting has attracted a lot of attention. In particular, the most effective electrocatalysts for the hydrogen evolution reaction (HER) in acidic media are Pt group metals, which possess high catalytic reaction rates and near-zero overpotential. However, their high price and extreme scarcity have posed tremendous limitations to widespread use. As a result, finding alternative catalysts which are earth-abundant, as well as highly efficient is a crucial step towards a sustainable "hydrogen economy".[9]

Recent studies have confirmed that transition metal chalcogenides, such as molybdenum and tungsten sulfide (MoS_x and WS_2, $x \approx 2$ to 3), will become promising candidates in the application of HER electrocatalysts.[10,11] MoS_2 possesses a lamellar hexagonal structure, in which the intra-layer Mo–S bonds are covalently bonded while the adjacent layers are weakly interacting by van der Waals forces.[12,13] It is reported that the hydrogen binding energy of MoS_2 is close to that of Pt, implying that MoS_2 can reduce protons at low overpotentials.[14,15] Furthermore, both experimental[16] and computational[14] studies have concluded that HER activity arises from the sites located along the edges of MoS_2 layers, while the basal surfaces are catalytically inert. As a result, emerging studies have sought to modulate the nanostructures of MoS_2 to maximally increase its exposure of active edge sites for catalysis.[17–20] For example, Jaramillo *et al.* designed a fully contiguous 3D mesoporous MoS_2 thin film, in which the double-gyroid structure can preferentially expose more catalytically active edge sites.[21] A scalable method was provided by Xie *et al.* to incorporate defects into MoS_2 surfaces, which led to partial cracking of the catalytically inert basal planes, and at the same time, engendered additional density of exposed active sites, thus resulting in a small onset potential of −120 mV with a Tafel slope of 50 mV per decade.[22]

Although increasing the number of active edge sites can improve the electrochemical performance of MoS_2, the poor intrinsic conductivity and anisotropic electrical transport of MoS_2 significantly impede its overall catalytic performance.

[a]State Key Laboratory of Molecular Engineering of Polymers, Department of Macromolecular Science, Fudan University, 220 Handan Road, Shanghai 200433, P. R. China. E-mail: txliu@fudan.edu.cn; Fax: +86-21-65640293; Tel: +86-21-55664197
[b]State Key Laboratory of Modification of Chemical Fibers and Polymer Materials, College of Materials Science and Engineering, Donghua University, 2999 North Renmin Road, Shanghai 201620, P. R. China. E-mail: 10110440003@fudan.edu.cn

† Electronic supplementary information (ESI) available. See DOI: 10.1039/c5ra27180k

Therefore, the key challenge to apply MoS_2 in the HER lies in the compensation for the conductivity while maintaining its nanosize. In this regard, forming highly dispersed and nanosized (*i.e.*, edge rich) MoS_2 on a conducting matrix is an ideal protocol to improve its catalytic activity for the HER. As a result, various conductive substrates, such as reduced graphene oxide,[23] carbon nanotubes (CNTs),[24] and 3D graphene foam[25,26] are chosen for mediating the growth of MoS_2, which not only efficiently prevents the aggregation of MoS_2, but also tremendously improves the conductivity of the whole composite material.

Among the various carbon materials, CNTs have been extensively studied in a wide range of applications due to their high electrical conductivity and good mechanical properties. However, for the structure with both ends closed, the inner surface and intra tube space of CNTs are chemically inert, which greatly restricts their potential in the energy conversion and storage field.[27–29] Consequently, it is meaningful to open the relatively closed structure of CNTs, especially for multi-walled CNTs (MWCNTs). Through longitudinally unzipping single or multi-walled CNTs, the tubular structure of CNTs can be opened up, thus obtaining graphene nanoribbons (GNRs). GNRs are quasi-one-dimensional, narrow and flat stripes of graphene, with the size confinement in two coordinates. Quasi-one-dimensional structures typically refer to some morphology, including nanowires, core–shell nanowires, nanotubes, nanobelts, nanoribbons, nanorods and nanorings.[30] Thanks to this unique geometry, the most striking characteristics of GNRs are their increased surface area and the abundant existence of exfoliated ribbon edge planes. As a kind of novel carbon nanomaterial, quasi-one-dimensional GNRs not only inherit many outstanding characteristics of traditional carbon materials, such as lightweight, high thermal conductivity, and excellent electrical conductivity, but also possess various interesting properties due to their distinctive edge sites, such as edge dependent electronic properties and variation in the band gap owing to electron confinement, which are the significant differences between CNTs and graphene.[31] Although there are many methods which can produce a microscopic specimen of GNRs, such as chemical vapor deposition (CVD),[32] and lithographic[33] and plasma etching,[34] they not only require precise equipment or harsh experimental conditions, but also cannot be used to produce GNRs with high yields and controlled widths.[35] Nevertheless, the solution-based oxidative procedure *via* longitudinal unzipping of MWCNTs followed by reduction is a simple, efficient, and scalable method to prepare GNRs, which is reported by Tour and co-workers.[36] The produced GNRs by this method possess excellent surface integration with fewer defects or holes on the basal plane and a high length-to-width ratio. Moreover, because of their unique architecture, quasi-one-dimensional GNRs also exhibit some novel capabilities in electrochemistry. For instance, GNRs exhibit enhanced electrochemical lithium storage performance as compared with other conventionally used carbon materials, which is attributed to the existence of a large number of edge sites.[37] Yi *et al.* prepared nitrogen-doped GNR aerogels as efficient electrocatalysts for the oxygen reduction reaction, in which GNRs make full use of their high electrical conductivity and endow extra catalytic sites without destroying the structural integrity.[38] A vertical MWCNT carpet was split to form a GNR carpet for application in supercapacitors. The splitting treatment increased the specific capacitance by about 4 times, which was largely induced by the enlarged specific surface area in the additional intra tube space and inner tube surface.[39] Therefore, these distinctive features of GNRs have made them promising candidates in electrochemical fields.

In this work, GNRs are employed as conductive substrates for the growth of few-layered MoS_2 nanosheets *via* a facile solvothermal method. In this hybrid, the increased surface space along with unzipped ribbon edges of the GNR sheets provide more sites for the anchoring of MoS_2, which greatly enlarges the exposed catalytic edge sites. Moreover, the intimate contact between the MoS_2 nanosheets and underlying GNR network further promotes fast electron transport from the less conductive MoS_2 nanosheets to the electrodes. Last but not least, the unzipping of MWCNTs into GNR sheets can benefit the permeation of the electrolyte, as the thinnish ribbon platelets make it easier for ion diffusion compared with the robust walls of MWCNTs. Therefore, the rationally designed GNR@MoS_2 hybrids exhibit excellent HER performance with a low onset potential of -0.11 V, large cathodic currents, as well as a small Tafel slope of 43.4 mV per decade. Besides preparing a GNR-based hybrid with a hierarchical structure as an efficient Pt-free catalyst in the HER, this report also extends the application of GNRs, making them a promising substrate in the electrochemical field.

2. Experimental section

2.1. Materials

MWCNTs are obtained from Chengdu Organic Chemicals Co. Ltd., produced by the chemical vapor deposition method with a diameter of 30–50 nm. Ammonium tetrathiomolybdate ($(NH_4)_2MoS_4$) was supplied by J&K Chemical. H_2SO_4 (95–98%), *N*,*N*-dimethylformamide (DMF, $\geq$99.5%) and ethanol were purchased from Shanghai Chemical Reagent Company. Potassium permanganate ($KMnO_4$) and hydrazine hydrate ($N_2H_4 \cdot H_2O$, 50 wt% in water) were supplied by China Medicine Company. Deionized (DI) water was used throughout all the experiments.

2.2. Preparation of GONR sheets

Graphene oxide nanoribbons (GONRs) were prepared by longitudinally unzipping MWCNTs through a simple solution-based oxidative process.[36] Typically, 150 mg pristine CNTs was suspended in 36 mL H_2SO_4, and stirred for 1 h to form a homogeneous dispersion. Then, 7 mL of phosphoric acid (H_3PO_4, 85 wt%) was added dropwise and stirred for another 30 min. 750 mg of $KMnO_4$ was gradually added and the mixture was under reaction at 70 °C for 2 h. After being cooled to room temperature naturally, the mixture was poured into 150 mL of ice water containing 7 mL of hydrogen peroxide (H_2O_2, 50 wt%). The product was allowed to coagulate overnight, and the

precipitate was washed with 10% HCl, followed by ethanol/ether several times. Finally, the suspension was centrifugated to obtain the solid products.

2.3. Preparation of GNR@MoS_2 hybrids

GNR@MoS_2 hybrids were synthesized through a facile solvothermal reaction according to Dai's method.[23] Briefly, 10 mg of GONRs was dispersed in 10 mL of DMF *via* sonication, followed by adding a certain amount of $(NH_4)_2MoS_4$ (11 mg, 22 mg, or 44 mg). The mixture was then sonicated to get a well-dispersed solution. 0.2 mL of $N_2H_4 \cdot H_2O$ was added into the solution, followed by sonication for another 30 min. After that, the mixture was transferred into a 40 mL Teflon-lined stainless steel autoclave to react at 200 °C for 12 h. The obtained products were collected by centrifugation at 12 000 rpm for 3 min and washed repeatedly with DI water and ethanol. Finally, the hybrids were dried at 60 °C for 12 h. The hybrids with different loading amounts of MoS_2 were denoted as GNR@MoS_2-0.5, GNR@MoS_2-1 and GNR@MoS_2-2, respectively (Scheme 1). For comparison, pure GNRs were prepared *via* the above method without the addition of $(NH_4)_2MoS_4$ while pure MoS_2 was prepared without GONRs. A physical mixture of GNRs and MoS_2 was also prepared and denoted as GNR&MoS_2. Acid-treated MWCNTs were used to synthesize the MWCNT@MoS_2 hybrid, with the same component ratio as the GNR@MoS_2-1 hybrid.

2.4. Characterization

The morphology of the products was observed using field emission scanning electron microscopy (FESEM, Ultra 55, Zeiss) at an acceleration voltage of 5 kV. EDS mapping images and the corresponding atomic ratio obtained from the mapping images were also obtained *via* field emission scanning electron microscopy (FESEM, Ultra 55, Zeiss) at an acceleration voltage of 10 kV. Transmission electron microscopy (TEM) and high-resolution transmission electron microscopy (HRTEM) were performed under an acceleration voltage of 200 kV with JEOL JEM2100 TEM. X-ray diffraction (XRD) experiments were conducted from $2\theta = 5°$ to 80° on an X'Pert Pro X-ray diffractometer with Cu Kα radiation ($\lambda = 0.1542$ nm) under a voltage of 40 kV and a current of 40 mA. Thermogravimetric analysis (Pyris 1 TGA) was performed under air flow from 100 to 700 °C at a heating rate of 20 °C min^{-1}. Raman spectra were measured on LabRam-1B French Dilor Com ($\lambda_{ex} = 532$ nm). X-ray photoelectron spectroscopy (XPS) analyses were made with Thermo Scientific ESCALAB 250Xi using an Al Kα source 1486.6 eV anode. All XPS spectra were corrected using the C 1s line at 284.6 eV. The Brunauer–Emmett–Teller (BET) surface area was measured using a Belsorp-max surface area detecting instrument by N_2 physisorption at 77 K.

2.5. Electrochemical measurements

4 mg of the GNR@MoS_2 hybrids was dispersed in 1 mL of 3 : 1 v/v water/ethanol along with 40 μL of 5 wt% Nafion solution, followed by sonication for 15 min to get a homogeneous slurry. Then 5 μL of the catalytic slurry was dropped onto a glassy carbon electrode (GCE) of 3 mm in diameter to form a GNR@MoS_2 modified GCE. For comparison, pure GNRs, MoS_2, GNR&MoS_2 and MWCNT@MoS_2 modified GCEs were also prepared in the same way.

All electrochemical tests were performed in a standard three-electrode setup using a CHI 660D electrochemical workstation (Shanghai Chenhua Instrument Co., China), where a graphite rod was used as the counter electrode, a saturated calomel electrode (SCE) as the reference electrode and the modified GCE as the working electrode. Linear sweep voltammetry (LSV) was measured with a scan rate of 5 mV s^{-1} in 0.5 M H_2SO_4. All polarization curves were corrected for IR loss and all of the potentials were calibrated to a reversible hydrogen electrode (RHE). The cycling stability was investigated by cyclic voltammetry (CV) between −0.35 and 0.25 V *vs.* RHE at a scan rate of 100 mV s^{-1}. AC impedance measurements were carried out with frequencies ranging from 10^6 Hz to 10^{-2} Hz with an amplitude of 5 mV.

3. Results and discussion

3.1. Morphology and structure of GNR@MoS_2 hybrids

The morphology of the pristine MWCNTs and unzipped GONRs is observed by TEM and SEM images, as shown in Fig. 1. Fig. 1A

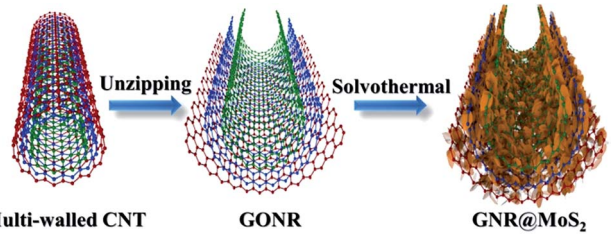

Scheme 1 Schematic illustration of the preparation of the GNR@MoS_2 hybrids.

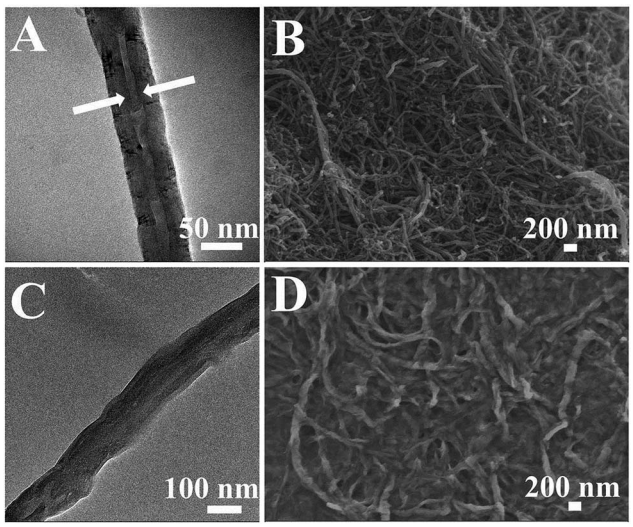

Fig. 1 TEM (left) and FESEM (right) images of (A and B) pristine CNTs, and (C and D) GONRs.

and C show the TEM images of the pristine MWCNTs and GONR sheets, respectively. The pristine MWCNTs display a diameter of 30–50 nm, along with clear boundaries of inner walls. After being unzipped by oxidizing agents, the GONR sheets show a layered structure, which is about 50–100 nm in width. The disappearance of a separatrix between the hollow cavities and inner walls, along with an enlarged width size indicates that the MWCNTs have been opened or unzipped longitudinally. The FESEM images of the MWCNTs and GONR sheets at low magnifications are shown in Fig. 1B and D. It can be observed that the opened GONR sheets possess a comparable length to that of the pristine MWCNTs, presenting a geometric structure with high aspect ratios and reduced defects.[40] The successful unzipping of the pristine MWCNTs can also be confirmed by the XRD patterns shown in Fig. S1.† The pristine MWCNTs display a characteristic peak at $2\theta = 26.1^\circ$, corresponding to a *d*-spacing of 3.4 Å. After unzipping, the GONRs show a predominant diffraction peak at $2\theta = 9.2^\circ$, corresponding to a *d*-spacing of 9.3 Å. The above results can adequately prove that the MWCNTs have been unzipped into GONRs. The BET specific surface area was further investigated by nitrogen isothermal adsorption. The specific surface area of the GONRs was calculated to be 209.6 $m^2\ g^{-1}$, which is much higher than that of the pristine MWCNTs (95.4 $m^2\ g^{-1}$). Compared with MWCNTs, the open structures and straight edges of the GONR sheets can benefit the interfacial contact with the electrolyte. Furthermore, this distinctive quasi-one-dimensional architecture can provide more exposed sites for the growth of MoS_2 nanosheets, which not only lies in the outer wall layer, but also exists in the unzipped inner wall, engendering a positive impact on the electrocatalytic performance.

In the solvothermal process, MoS_2 nanosheets are decorated onto the surface of the GONR sheets with different loading amounts while the GONRs are reduced to GNRs by N_2H_4 at the same time. The morphology of the GNR@MoS_2 hybrids is shown in Fig. 2. It can be seen in Fig. 2A and B that ultrathin MoS_2 nanosheets are decorated onto the GNRs, forming the crumpled edges in the GNR@MoS_2-0.5 hybrid. However, there are still some exposed GNRs not fully covered by the MoS_2 nanosheets. For GNR@MoS_2-1, the layered MoS_2 nanosheets are uniformly distributed on the GNR surface, forming a three-dimensional (3D) network (Fig. 2C and D). The unique structure of the quasi-one-dimensional GNRs with unzipped ribbon edges can provide more active sites for the growth of MoS_2, thus enhancing the electrocatalytic performance. The EDS mapping images of GNR@MoS_2-1 are shown in Fig. S2,† which confirms that the MoS_2 nanosheets are distributed evenly on the GNRs and the molar ratio of S to Mo is about 2 : 1. With the increase of the amount of $(NH_4)_2MoS_4$ precursor (Fig. 2E and F), the MoS_2 nanosheet layers tend to become thicker and some aggregations appear on the surface of the GNRs in the GNR@MoS_2-2 hybrid. For pure MoS_2 without the GNR template (Fig. S3A†), it can be observed that MoS_2 seriously aggregates into a hydrangea-like morphology, which greatly hinders the exposure of the catalytically active edge sites of MoS_2. Fig. S3B† displays the morphology of the GNR sheets produced in the same solvothermal reaction without the addition of $(NH_4)_2MoS_4$. After

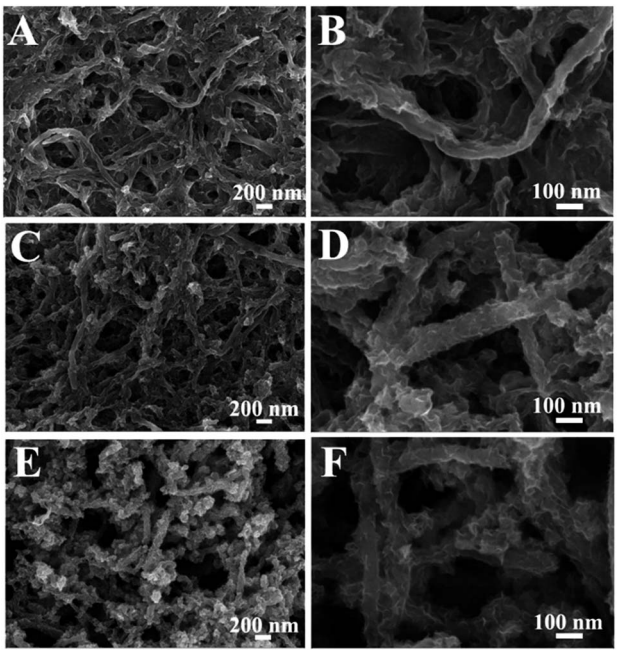

Fig. 2 FESEM images of the (A and B) GNR@MoS_2-0.5, (C and D) GNR@MoS_2-1, and (E and F) GNR@MoS_2-2 hybrids at low (left) and high (right) magnifications.

reduction with N_2H_4, the GNR sheets become a little frizzy, which may result from the removal of oxygen-containing groups.

The detailed microstructure of the GNR@MoS_2-1 hybrid was further confirmed by TEM observations, as shown in Fig. 3. The surface of the GNR sheets is fully covered with curly ultrathin MoS_2 nanosheets, which is in good accordance with the FESEM observations (Fig. 2C and D). In addition, it can be obviously found that the fully exfoliated ribbon edges are also anchored with some corrugated MoS_2 nanosheets (white arrows in Fig. 3A), extending from the strip-like basal plane, which offers additional active sites for the growth of MoS_2, making full utilization of the unique quasi-one-dimensional structure of the GNR nanosheets. The HRTEM image in Fig. 3B further elucidates that the MoS_2 nanosheets are composed of 5–7 sandwiched S–Mo–S layers, along with an inter-layer spacing of 0.69

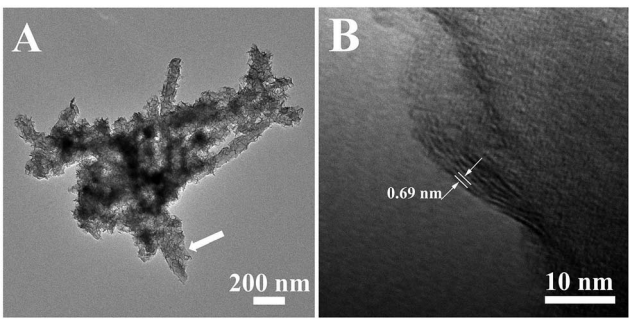

Fig. 3 TEM images of the GNR@MoS_2-1 hybrid at (A) low and (B) high magnification.

nm. In order to make a more distinct comparison, the morphology of the MWCNT@MoS_2 hybrid is displayed in Fig. S4.† Comparing the two images, it can be obviously observed that the average width of GNR@MoS_2-1 is larger than that of MWCNT@MoS_2, which is generated by fully unzipping the tube walls of the MWCNTs. As a result, more active sites, both the outer and inner wall surfaces, are presented in the GNR sheets for the decoration of the MoS_2 sheets as compared with that of the MWCNTs. Naturally, with the same amount of $(NH_4)_2MoS_4$ precursor, the MoS_2 sheets grow more densely and closely on the substrate of the quasi-one-dimensional GNR sheets with a large number of extra growth sites originating from the unzipping process. On the contrary, the MWCNTs only provide the space of the outer wall for the decoration of MoS_2 sheets, which can be verified by the TEM image, where the trace of the inner wall boundaries could still be slightly tracked even after the growth of the MoS_2 sheets (white arrows in Fig. S4†).

XRD patterns of the GNRs, pure MoS_2 and the GNR@MoS_2 hybrids are displayed in Fig. 4. Different from the GONRs showing a diffraction peak at $2\theta = 9.2°$ in Fig. S1,† the pattern of the GNRs displays a broad peak at $2\theta = 25.8°$, indicating that the inter-layer space of the GNRs is decreased due to the removal of oxygen-containing groups. A similar phenomenon has been reported for the case of graphene.[41] As for pure MoS_2, two broad peaks at $2\theta = 32.8°$ and 57.3° can be indexed to the (100) and (110) diffraction planes of 2H-MoS_2, while two peaks at $2\theta = 9.6°$ and 18.6° indicate oxygen-incorporated MoS_2 ultrathin nanosheets, which can dramatically enhance the HER activity compared with the pristine 2H-MoS_2 (JCPDS Card No. 73-1508).[42] As for the GNR@MoS_2 hybrids, some characteristic diffraction peaks of MoS_2 can be observed, while the absence of peaks at the low-angle region indicates that the MoS_2 nanosheets are not restacked at all, which is advantageous for the HER activity.[24] Besides, the absence of diffraction peaks for the GNRs in the hybrids may be ascribed to the relatively higher intensity of the diffraction peaks of MoS_2.

To further confirm the reduction of the GNRs in the hybrids, Raman spectra are measured, as shown in Fig. S5.† The D band at 1363 cm^{-1} refers to a breathing mode of the κ-point photons of A_{1g} symmetry while the G band at 1594 cm^{-1} corresponds to the first-order scattering of the E_{2g} mode.[43] It can be clearly observed that after reduction by N_2H_4, an increased D/G intensity ratio appears both in the curves of the pure GNRs and the GNR@MoS_2-1 hybrid as compared with the GONRs, which is similar to what has been reported for graphene oxide.[44] Thus, the increased number of small domains of aromaticity may be responsible for the enhanced D band.[45]

XPS spectra were further investigated to confirm the compositions and chemical states of the GNR@MoS_2 hybrids. Fig. 5A reveals the co-existence of C, Mo, S and O elements in the products, without any detectable impurities. The high-resolution Mo 3d spectrum (Fig. 5B) presents two major peaks at 228.9 eV and 232.0 eV, corresponding to the binding energies of Mo $3d_{3/2}$ and Mo $3d_{5/2}$, characteristic of Mo^{4+} in MoS_2, indicating the dominance of Mo(IV) in the GNR@MoS_2 products.[46] A small peak can be observed at 225.8 eV, which is attributed to the S 2s component in MoS_2. Fig. 5C shows the high-resolution S 2p spectrum, and the peaks located at 162.9 eV and 161.8 eV refer to S $2p_{1/2}$ and S $2p_{3/2}$ orbits of divalent sulfide ions (S^{2-}), respectively.[47] The above results further prove the successful growth of MoS_2 nanosheets onto the surface of the GNRs. Fig. 5D presents the high-resolution C 1s spectrum of the GNR@MoS_2-1 hybrid, showing a standard carbon peak at 284.6 eV. The loading percentages of MoS_2 in the hybrids can be estimated from the TGA curves (Fig. S6†), being 25.3%, 39.2% and 49.4% for the GNR@MoS_2-0.5, GNR@MoS_2-1 and GNR@MoS_2-2 hybrids, respectively.

3.2. HER electrocatalytic activity of the GNR@MoS_2 hybrids

The electrocatalytic HER activity of the GNR@MoS_2 hybrids was investigated in 0.5 M H_2SO_4 solution using a typical three-electrode setup. Fig. 6 shows the LSV curves for the GNR@MoS_2 hybrids with different MoS_2 loading percentages. It is universally acknowledged that an excellent HER catalyst should generate the highest amount of hydrogen at the lowest

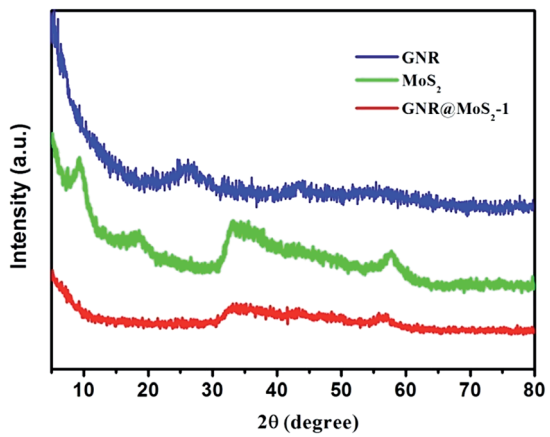

Fig. 4 XRD patterns of the GNRs, MoS_2 and the GNR@MoS_2-1 hybrid.

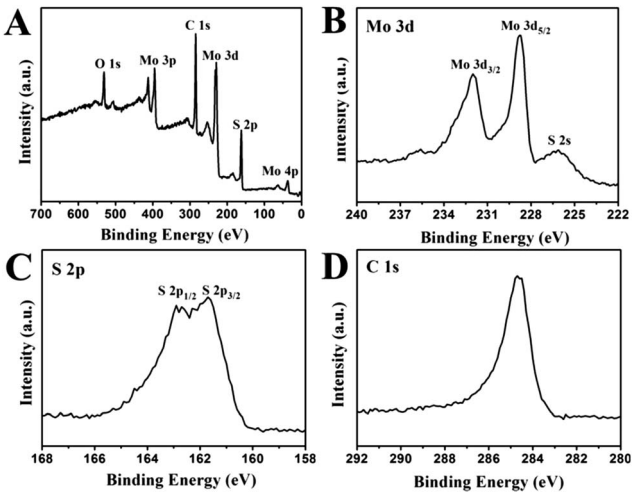

Fig. 5 XPS spectra of the GNR@MoS_2-1 hybrid: (A) survey spectrum, and high-resolution (B) Mo 3d, (C) S 2p, and (D) C 1s spectra.

overpotential. As a result, it can be observed that among the GNR@MoS_2 hybrids, the GNR@MoS_2-1 modified GCE exhibits the optimal HER catalytic performance, with significant hydrogen evolution ($J = 10$ mA cm^{-2}) observed at a voltage as low as −180 mV. The other two curves are more or less negatively shifted, indicating a poorer HER performance. The difference of electrocatalytic activity between the hybrids with different MoS_2 loading percentages can be explained as follows: for the GNR@MoS_2-0.5 hybrid, thinnish MoS_2 sheets are sparsely decorated on the GNR template, and some regions of the GNRs are exposed without the coverage of active HER catalysts. In contrast, an overloaded amount of MoS_2 nanosheets is overspread on the GNR templates in the GNR@MoS_2-2 hybrid, resulting in an inevitable aggregation of MoS_2. As is well known, the HER activity of MoS_2 arises from the exposure of active edge sites, *i.e.*, its co-ordinated sulfur edge sites. As for GNR@MoS_2-2, on the one hand, the thick layer of MoS_2 nanosheets decreases the number of catalytically active edge sites. On the other hand, the agglomerates severely prevent the ion transport and electron transfer during the HER process. Consequently, the GNR@MoS_2-1 hybrid displays the optimal HER catalytic activity.

The comparison of HER performance between the pure GNRs, MoS_2, GNR&MoS_2, MWCNT@MoS_2 and the GNR@MoS_2-1 hybrid is also investigated. As shown in Fig. 7A, the pure GNR sheets display an almost negligible HER activity with a horizontal line against the potential. Although both pure MoS_2 and GNR&MoS_2 exhibit distinct electrocatalytic ability, the current density and onset potential are far beyond those of the GNR@MoS_2-1 hybrid, which may be due to the poor conductivity, limited exposed active edges and the insufficient contact between the GNR template and the electro-active MoS_2 sheets. On the whole, the largely enhanced catalytic HER performance of the GNR@MoS_2 hybrids can be attributed to the synergistic effect between the highly conductive GNRs and the electro-active MoS_2 nanosheets, indicating the successful construction of the hybrid materials. In addition, it is worth mentioning that MWCNT@MoS_2 exhibits significantly worse HER activity

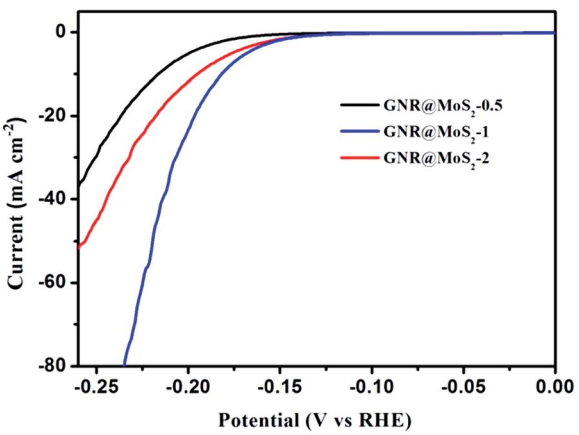

Fig. 6 LSV polarization curves for the GNR@MoS_2-0.5, GNR@MoS_2-1 and GNR@MoS_2-2 modified GCEs in N_2-purged 0.5 M H_2SO_4 solution.

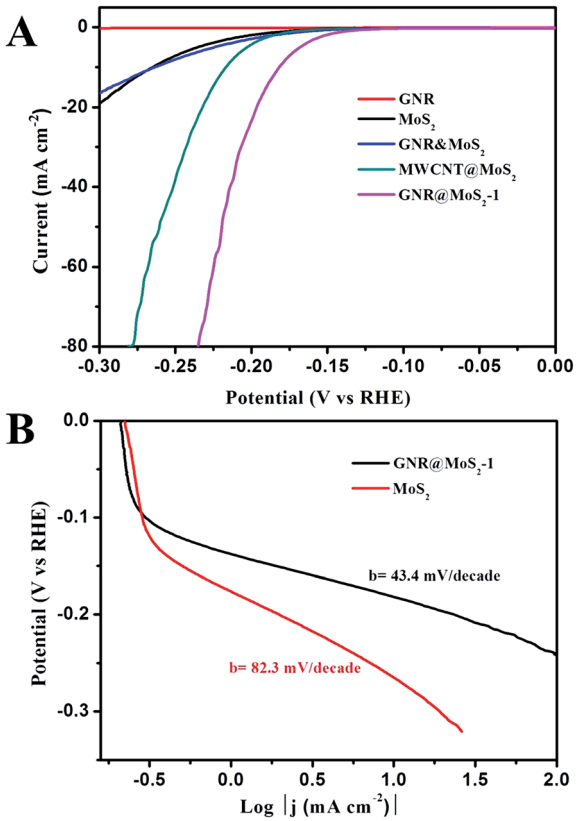

Fig. 7 (A) LSV polarization curves for different material modified GCEs in N_2-purged 0.5 M H_2SO_4 solution. (B) Tafel plots for the pure MoS_2 and GNR@MoS_2-1 modified GCE.

compared with that of GNR@MoS_2-1, with a current density of 10 mA cm^{-2} at a voltage of −216 mV. The relatively poor catalytic performance for MWCNT@MoS_2 may be due to the limited space of the outer wall of the MWCNTs for the growth of the MoS_2 nanosheets, not taking full utilization of the inner surface or intra tube space, which can also be speculated from their morphological difference as discussed above. Moreover, MWCNTs with closed ends are also unfavorable for the electrolyte permeation, leading to inferior electrochemical activity.

The Tafel slope, an inherent property of the catalyst, is related to the reaction mechanism of a catalyst and determined by the rate-limiting step of the HER.[11] The onset potential for the HER is determined from the semi-log plot, which is the starting point of the linear relationship of the Tafel curve. It is observed in Fig. 7B that the GNR@MoS_2-1 hybrid displays superb HER activity with a low onset potential of −0.11 V, which surpasses that of pure MoS_2. The Tafel slope can be deduced from the Tafel equation ($\eta = b\log(j) + a$, where η is the overpotential, j is the current density, and b is the Tafel slope), yielding Tafel slopes of 43.4 and 82.3 mV per decade for GNR@MoS_2-1 and pure MoS_2, respectively.

In terms of the mechanism of hydrogen evolution, the Tafel slope of GNR@MoS_2-1 indicates that the HER process takes place *via* a rapid Volmer reaction, followed by a rate-limiting Heyrovsky reaction.[48,49] The HER performance of the GNR@MoS_2 hybrids is comparable or superior to some

previously reported MoS_2-based HER catalysts, as listed in Table S1.† The extraordinary HER ability can be elucidated with the schematic diagram shown in Fig. 8. First, the GNR sheets not only serve as a conducting template, but also provide more surface area for the growth of MoS_2, that is, both in the outer sheets and inner wall layers, as well as the edges along the quasi-one-dimensional strips. Second, the thin strips of quasi-one-dimensional GNRs are beneficial for the permeation of the electrolyte, which is rather different from the MWCNTs with relatively thicker walls. Third, the GNRs can form a highly conductive pathway, which facilitates the transportation of electrons. Last but not least, an appropriate amount of MoS_2 nanosheets is decorated onto the GNRs through controllable adjustment of the morphology, thus effectively preventing the self-agglomeration of MoS_2 and excessive exposure of the GNRs, taking full advantages of both components.

Electrochemical impedance spectroscopy (EIS) is a useful technique to evaluate the interface reactions and catalytic kinetics in the HER process. The Nyquist plots of the pure GNR, MoS_2, MWCNT@MoS_2 and GNR@MoS_2-1 modified GCEs are displayed in Fig. 9A. The solution resistance R_s can be obtained from the intersection of the curves at the real axis in the range of the high frequency region while the charge transfer resistance R_{ct} corresponds to the semicircle of the Nyquist plots. A straight line in the low frequency region and an inconspicuous arc in the high frequency region are shown in the Nyquist plot of GNR@MoS_2-1, revealing a dramatically decreased R_s and R_{ct} for the GNR@MoS_2 hybrids compared with those for pure MoS_2. It further implies that the GNRs can shorten the pathway of ion diffusion and facilitate the electron transfer, which gives prominence to the important function of a highly conductive template with a large surface area. For MWCNT@MoS_2, it can be observed that its solution resistance R_s is apparently larger than that of GNR@MoS_2-1, indicating poor contact between the electrolyte ions and hybrid material. More importantly, the semicircle of MWCNT@MoS_2 is more obvious in comparison with that of the GNR@MoS_2-1 hybrid (Fig. S7†), illustrating its higher charge resistance during the electrocatalytic process. As a result, the template of the GNRs indeed plays a critically significant role of facilitating the permeation of the electrolyte, which can be ascribed to the thinnish ribbon strips of the quasi-one-dimensional GNRs, providing an open space during the HER performance compared with the relatively closed structure of the muti-walled CNTs.

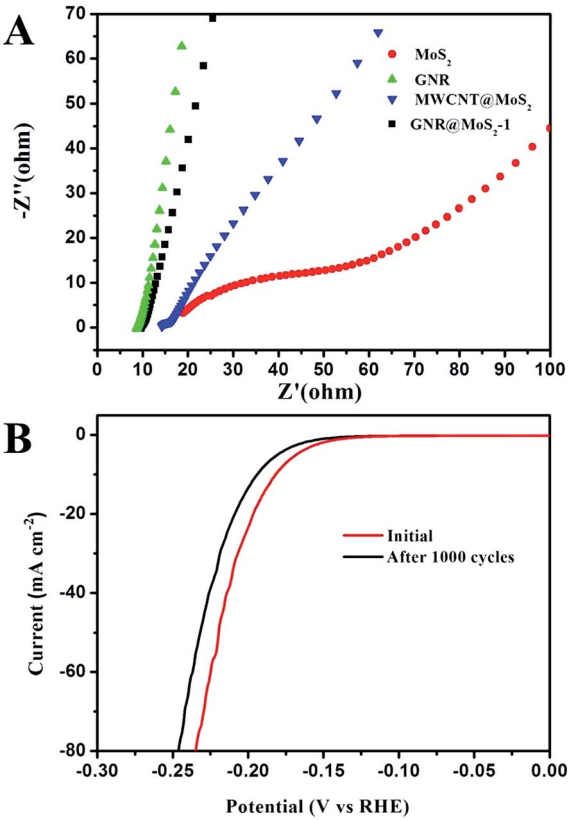

Fig. 9 (A) Nyquist plots for the GNRs, MoS_2, MWCNT@MoS_2 and GNR@MoS_2-1 hybrid. (B) LSV polarization curves for the GNR@MoS_2-1 modified GCE recorded before and after 1000 CV cycles.

The durability of the GNR@MoS_2-1 catalyst was also investigated using CV measurements by scanning 1000 cycles from −0.35 V to 0.25 V (*vs.* RHE) with a scan rate of 100 mV s^{-1} in 0.5 M H_2SO_4. As shown in Fig. 9B, it can be observed that the polarization curve after cycling displays a slight negative shift, which may be caused by the inevitable partial decrease of active edges of MoS_2 for the HER.

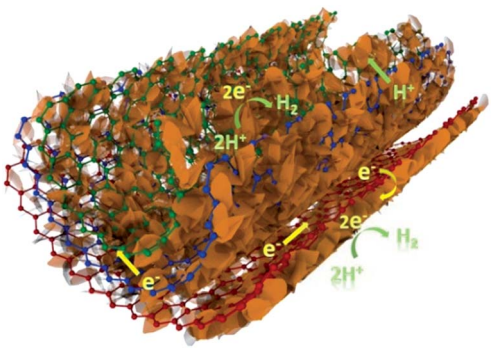

Fig. 8 Schematic diagram of the GNR@MoS_2 hybrids for the hydrogen evolution reaction.

4. Conclusions

In summary, few-layered MoS_2 nanosheet-decorated GNR hybrids with heterostructures have been synthesized through a simple oxidative unzipping process combined with a one-step solvothermal reaction. Due to the unique structure of quasi-one-dimensional GNRs with enlarged surface area and distinct unzipped edges, an increased number of electrocatalytic active edge sites of MoS_2 can be exposed. Furthermore, GNRs featured with high length-to-width ratios provide a highly conductive network for the electron transport while their exfoliated thinnish sheets supply a convenient pathway for the ion diffusion. As a result, the rationally designed GNR@MoS_2 hybrid exhibits outstanding HER activity with a large current density (10 mA cm^{-2} at η = 180 mV), a relatively low onset

potential of −0.11 V, and a small Tafel slope of 43.4 mV per decade. Apart from preparing nanostructured GNR@MoS_2 hybrids for efficient Pt-free HER catalysts, this study also emphasizes the functions of GNRs as a conducting matrix, which may become a promising substrate in fabricating hybrid nanomaterials for electrochemistry.

Acknowledgements

The authors are grateful for the financial support from the National Natural Science Foundation of China (51125011, 51433001).

Notes and references

1 S. Chu and A. Majumdar, *Nature*, 2012, **488**, 294–303.
2 N. Muradov and T. Veziroglu, *Int. J. Hydrogen Energy*, 2008, **33**, 6804–6839.
3 J. Greeley, T. F. Jaramillo, J. Bonde, I. B. Chorkendorff and J. K. Norskov, *Nat. Mater.*, 2006, **5**, 909–913.
4 W. F. Chen, J. T. Muckerman and E. Fujita, *Chem. Commun.*, 2013, **49**, 8896–8909.
5 N. Zhang, M.-Q. Yang, S. Q. Liu, Y. G. Sun and Y.-J. Xu, *Chem. Rev.*, 2015, **115**, 10307–10377.
6 M.-Q. Yang, C. Han and Y.-J. Xu, *J. Phys. Chem. C*, 2015, **119**, 27234–27246.
7 N. Zhang, Y. H. Zhang and Y.-J. Xu, *Nanoscale*, 2012, **4**, 5792–5813.
8 C. Han, Z. Chen, N. Zhang, J. C. Colmenares and Y.-J. Xu, *Adv. Funct. Mater.*, 2015, **25**, 221–229.
9 D. Merki and X. L. Hu, *Energy Environ. Sci.*, 2011, **4**, 3878–3888.
10 D. Voiry, H. Yamaguchi, J. W. Li, R. Silva, D. C. B. Alves, T. Fujita, M. W. Chen, T. Asefa, V. B. Shenoy, G. Eda and M. Chhowalla, *Nat. Mater.*, 2013, **12**, 850–855.
11 Y. Yan, B. Y. Xia, Z. C. Xu and X. Wang, *ACS Catal.*, 2014, **4**, 1693–1705.
12 M. Chhowalla, H. S. Shin, G. Eda, L. J. Li, K. P. Loh and H. Zhang, *Nat. Chem.*, 2013, **5**, 263–275.
13 B. Radisavljevic, A. Radenovic, J. Brivio, V. Giacometti and A. Kis, *Nat. Nanotechnol.*, 2011, **6**, 147–150.
14 B. Hinnemann, P. G. Moses, J. Bonde, K. P. Jørgensen, J. H. Nielsen, S. Horch, I. Chorkendorff and J. K. Nørskov, *J. Am. Chem. Soc.*, 2005, **127**, 5308–5309.
15 A. B. Laursen, S. R. Kegnæs, S. R. Dahl and I. Chorkendorff, *Energy Environ. Sci.*, 2012, **5**, 5577–5591.
16 T. F. Jaramillo, K. P. Jørgensen, J. Bonde, J. H. Nielsen, S. Horch and I. Chorkendorff, *Science*, 2007, **317**, 100–102.
17 H. L. Yu, X. B. Yu, Y. J. Chen, S. Zhang, P. Gao and C. Y. Li, *Nanoscale*, 2015, **7**, 8731–8738.
18 Y. P. Huang, Y. E. Miao, L. S. Zhang, W. W. Tjiu, J. S. Pan and T. X. Liu, *Nanoscale*, 2014, **6**, 10673.
19 X. Zhao, H. Zhu and X. R. Yang, *Nanoscale*, 2014, **6**, 10680–10685.
20 J. X. Guo, F. F. Li, Y. F. Sun, X. Zhang and L. Tang, *J. Power Sources*, 2015, **291**, 195–200.
21 J. Kibsgaard, Z. Chen, B. N. Reinecke and T. F. Jaramillo, *Nat. Mater.*, 2012, **11**, 963–969.
22 J. F. Xie, H. Zhang, S. Li, R. X. Wang, X. Sun, M. Zhou, J. F. Zhou, X. W. Lou and Y. Xie, *Adv. Mater.*, 2013, **25**, 5807–5813.
23 Y. G. Li, H. L. Wang, L. M. Xie, Y. Y. Liang, G. S. Hong and H. J. Dai, *J. Am. Chem. Soc.*, 2011, **133**, 7296–7299.
24 Y. Yan, X. M. Ge, Z. L. Liu, J. Y. Wang, J. M. Lee and X. Wang, *Nanoscale*, 2013, **5**, 7768.
25 L. Liao, J. Zhu, X. J. Bian, L. Zhu, M. D. Scanlon, H. H. Girault and B. H. Liu, *Adv. Funct. Mater.*, 2013, **23**, 5326–5333.
26 X. Zhang, Q. W. Zhang, Y. F. Sun, P. Y. Zhang, X. Gao, W. Zhang and J. X. Guo, *Electrochim. Acta*, 2016, **189**, 224–230.
27 S. R. Wang, Z. Y. Liang, B. Wang, C. Zhang and Z. Rahman, *Nanotechnology*, 2007, **18**, 055301.
28 C. J. Zhang, H. H. Zhou, X. Q. Yu, D. Shan, T. T. Ye, Z. Y. Huang and Y. F. Kuang, *RSC Adv.*, 2014, **4**, 11197–11205.
29 H. W. Wang, Y. L. Wang, Z. A. Hu and X. F. Wang, *ACS Appl. Mater. Interfaces*, 2012, **4**, 6827–6834.
30 E. Comini, C. Baratto, G. Faglia, M. Ferroni, A. Vomiero and G. Sberveglieri, *Prog. Mater. Sci.*, 2009, **54**, 1–67.
31 O. V. Yazyev, *Acc. Chem. Res.*, 2013, **46**, 2319–2328.
32 J. Campos-Delgado, J. M. Romo-Herrera, X. T. Jia, D. A. Cullen, H. Muramatsu, Y. A. Kim, T. Hayashi, Z. F. Ren, D. J. Smith, Y. Okuno, T. Ohba, H. Kanoh, K. Kaneko, M. Endo, H. Terrones, M. S. Dresselhaus and M. Terrones, *Nano Lett.*, 2008, **8**, 2773–2778.
33 L. Tapaszto, G. Dobrik, P. Lambin and L. P. Biro, *Nat. Nanotechnol.*, 2008, **3**, 397–401.
34 L. Y. Jiao, L. Zhang, X. R. Wang, G. Diankov and H. J. Dai, *Nature*, 2009, **458**, 877–880.
35 M. K. Liu, Y. F. Song, S. X. He, W. W. Tjiu, J. S. Pan, Y. Y. Xia and T. X. Liu, *ACS Appl. Mater. Interfaces*, 2014, **6**, 4214–4222.
36 A. L. Higginbotham, D. V. Kosynkin, A. Sinitskii, Z. Z. Sun and J. M. Tour, *ACS Nano*, 2010, **4**, 2059–2069.
37 T. Bhardwaj, A. Antic, B. Pavan, V. Barone and B. D. Fahlman, *J. Am. Chem. Soc.*, 2010, **132**, 12556–12558.
38 L. Chen, R. Du, J. H. Zhu, Y. Y. Mao, C. Xue, N. Zhang, Y. L. Hou, J. Zhang and T. Yi, *Small*, 2015, **11**, 1423–1429.
39 C. G. Zhang, Z. W. Peng, J. Lin, Y. Zhu, G. D. Ruan, C. Hwang, W. Lu, R. H. Hauge and J. M. Tour, *ACS Nano*, 2013, **7**, 5151–5159.
40 M. K. Liu, W. W. Tjiu, J. S. Pan, C. Zhang, W. Gao and T. X. Liu, *Nanoscale*, 2014, **6**, 4233.
41 L. H. Tang, Y. Wang, Y. M. Li, H. B. Feng, J. Lu and J. H. Li, *Adv. Funct. Mater.*, 2009, **19**, 2782–2789.
42 J. F. Xie, J. J. Zhang, S. Li, F. Grote, X. D. Zhang, H. Zhang, R. X. Wang, Y. Lei, B. C. Pan and Y. Xie, *J. Am. Chem. Soc.*, 2013, **135**, 17881–17888.
43 F. Tuinstra and J. L. Koenig, *J. Chem. Phys.*, 1970, **53**, 1126–1130.
44 S. Stankovich, D. A. Dikin, R. D. Piner, K. A. Kohlhaas, A. Kleinhammes, Y. Y. Jia, Y. Wu, S. T. Nguyen and R. S. Ruoff, *Carbon*, 2007, **45**, 1558–1565.

45 M. A. Rafiee, W. Lu, A. V. Thomas, A. Zandiatashbar, J. Rafiee, J. M. Tour and N. A. Koratkar, *ACS Nano*, 2010, **4**, 7415–7420.
46 S. S. Ji, Z. Yang, C. Zhang, Z. Y. Liu, W. W. Tjiu, I. Y. Phang, Z. Zhang, J. S. Pan and T. X. Liu, *Electrochim. Acta*, 2013, **109**, 269–275.
47 P. P. Wang, H. Y. Sun, Y. J. Ji, W. H. Li and X. Wang, *Adv. Mater.*, 2014, **26**, 964–969.
48 J. O. Bockris and E. C. Potter, *J. Electrochem. Soc.*, 1952, **99**, 169–186.
49 B. E. Conway and B. V. Tilak, *Electrochim. Acta*, 2002, **47**, 3571–3594.